

Article

Structural and Catalytic Characterization of $\text{La}_{0.6}\text{Sr}_{0.4}\text{MnO}_3$ Nanofibers for Application in Direct Methane Intermediate Temperature Solid Oxide Fuel Cell Anodes

Enrico Squizzato ¹, Caterina Sanna ², Antonella Glisenti ¹ and Paola Costamagna ^{2,*}

¹ Department of Chemical Sciences, University of Padova, Via F. Marzolo 1, 35131 Padova, Italy; enrico.squizzato.1@phd.unipd.it (E.S.); antonella.glisenti@unipd.it (A.G.)

² Department of Chemistry and Industrial Chemistry, University of Genoa, Via Dodecaneso 31, 16146 Genoa, Italy; caterina.sanna@edu.unige.it

* Correspondence: paola.costamagna@unige.it; Tel.: +39-(0)10-3532922; Fax: +39-(0)10-3538733

Abstract: In the present work, structural and catalytic characterization was performed on $\text{La}_{0.6}\text{Sr}_{0.4}\text{MnO}_3$ (LSM) nanofibers. The LSM nanofibers were obtained using the electrospinning technique. For comparison, LSM powders with identical composition were characterized as well. The LSM powders were prepared through a self-combustion citrate-based procedure. SEM, EDX, XRD, and BET investigations were carried out on both LSM nanofibers and powders, pointing out the different structural features. The LSM nanofibers showed a higher surface area than the LSM powders and a lower presence of strontium oxide on the surface. Results of the H_2 -Temperature Programmed Reduction (TPR) tests showed evidence of a higher reactivity of the nanofibers compared to the powders. The catalytic characterization was performed utilizing a methane oxidation activity test, revealing a better catalytic performance of the LSM nanofibers: at 800 °C. The methane conversion achieved with the LSM nanofibers was 73%, which compared well with the 50% obtained with powders at 900 °C.

Keywords: electrospinning; nanofibers; fuel anode; H_2 -Temperature Programmed Reduction (TPR); Intermediate Temperature-Solid Oxide Fuel Cell (IT-SOFC)



Citation: Squizzato, E.; Sanna, C.; Glisenti, A.; Costamagna, P. Structural and Catalytic Characterization of $\text{La}_{0.6}\text{Sr}_{0.4}\text{MnO}_3$ Nanofibers for Application in Direct Methane Intermediate Temperature Solid Oxide Fuel Cell Anodes. *Energies* **2021**, *14*, 3602. <https://doi.org/10.3390/en14123602>

Academic Editor: Vladislav A. Sadykov

Received: 27 May 2021
Accepted: 10 June 2021
Published: 17 June 2021

Publisher's Note: MDPI stays neutral with regard to jurisdictional claims in published maps and institutional affiliations.



Copyright: © 2021 by the authors. Licensee MDPI, Basel, Switzerland. This article is an open access article distributed under the terms and conditions of the Creative Commons Attribution (CC BY) license (<https://creativecommons.org/licenses/by/4.0/>).

1. Introduction

Fuel cells are electrochemical devices that directly convert the chemical energy of the fuel into electrical energy, avoiding the Carnot cycle and allowing high efficiencies to be achieved [1,2]. For this reason—and due to the constant increase in energy demand and consequently in greenhouse gas emissions—fuel cells have drawn great attention over the last few decades. Among all fuel cell configurations, intermediate temperature solid oxide fuel cells (IT-SOFCs) have solid-state components. These offer wide fuel flexibility, since they can operate with both hydrogen and light hydrocarbons [3,4]. The latter is an interesting feature, since natural gas and methane are cheap and abundant fuels, whereas pure hydrogen is mostly produced through the hydrocarbon reforming process [5–7]. In the SOFC anode, methane can either be electro-oxidized directly or undergo an internal reforming process in which methane is converted into hydrogen. Both options have been investigated in recent years [8,9]. The internal methane reforming process is generally carried out employing nickel-based electrodes. The main challenges of this process are controlling temperature gradients across the SOFC stacks and avoiding coke deposition over the nickel catalyst, with consequent catalyst deactivation. The previous issue is due to the strong endothermicity of the methane steam reforming reaction, resulting in uneven temperature distribution over the cell, with the possible formation of cold spots [6]. The latter issue is behind the need to operate the cell with a steam-to-carbon (S/C) ratio larger than three, which makes it difficult to achieve complete methane conversion [9]. Due to these problems, IT-SOFCs running internal steam methane reforming processes require

high costs and complex balance-of-plant (BoP) components. The direct electro-oxidation of methane represents an interesting alternative. The direct utilization of methane provides high open-circuit voltage, with high efficiency and simple BoP [8,10,11]. Nevertheless, the direct electrochemical oxidation of methane cannot be carried out employing standard nickel-based electrodes. Indeed, at an operating temperature above 800 °C, severe coke deposition takes place. At temperatures below 800 °C, the nickel-based anode provides low power densities [12]. Nevertheless, it is possible to use innovative anode materials. Interesting improvements have been made employing anode materials containing Cu, which does not catalyze the formation of graphite [9,10]. Another option is perovskite materials, which have been widely investigated in SOFC applications as both anode and cathode. The ideal perovskite, represented with the ABO_3 general formula, is a versatile metal oxide. It can be doped in both the A and B sites, affecting the oxygen stoichiometry and improving the oxygen ion—as well as the electron conductivity [13–18]. One state-of-the-art perovskite for SOFC cathode application is the Sr-doped $LaMnO_3$. Lanthanum substitution with strontium in the A-site results in an increase of electronic conductivity from 83 S cm^{-1} for $LaMnO_3$ to 320 S cm^{-1} for $La_{0.6}Sr_{0.4}MnO_3$ (LSM), at the same operating temperature of 800 °C [19]. The same type of material ($La_{0.8}Sr_{0.2}Mn_{0.98}O_3$) has also been studied for oxidative coupling of methane in solid oxide membrane reactors [20]. Conductive perovskites—such as $(La,Sr)(Cr,Mn)O_3/(Ce,Gd)_{2-\delta}$ —have been tested in fuel cells with a direct methane configuration, reporting a polarization resistance of $0.496 \text{ } \Omega\text{cm}^2$ at 850 °C [21].

In addition to new materials, innovative electrode architectures have been investigated as well. One-dimensional (1D) nanomaterials, like nanofibers and nanorods, have been widely studied as promising electrode structures [22–28]. Nanofiber electrodes feature a high void degree and active surface. The nanofiber manufacture process is carried out by applying a high voltage between a metal precursor solution, injected through a syringe equipped with a metal needle, and a metal collector. In order to achieve proper nanofiber formation, several equipment and solution parameters must be optimized. In particular, the solution flow rate, the applied voltage, the collector rotation speed, and the environment-relative humidity may affect the final nanofiber structure. On the other hand, once the process parameters are optimized, the results are reproducible [29–32]. Overall, nanofiber-based electrodes are expected to show better electrochemical performance than common powder ones. The two different architectures were investigated through the electrochemical impedance spectroscopy test (EIS), and the nanofiber-based electrode reported lower polarization resistance [33]. Nevertheless, the structural and microstructural origin of this behavior has, to date, received little attention.

In this work, our aim was to understand how the structure and morphology of the material affects its capability in activating and oxidating methane. The specific surface area is not the only aspect that can deeply differ from powder to fibers; the surface composition can be severely modified by the synthesis procedure, and can play a relevant role. Methane oxidation was selected as a model reaction because it is not easily promoted by perovskites or Ni-free catalysts. Moreover, this is a reaction of high technological impact; its application in direct methane IT-SOFCs is just one example. LSM electrospun nanofibers and powders were synthesized, and particular attention was paid to the optimization of the fiber procedure. The obtained materials were investigated using X-Ray Diffraction (XRD), Scanning Electron Microscopy (SEM), Energy Dispersive X-Ray Spectroscopy (EDX), and N_2 -Physisorption. Particular care was devoted to the study of the surface using X-Ray Photoelectron Spectroscopy (XPS). The H_2 -Temperature Programmed Reduction (TPR) and methane oxidation activity tests were carried out to investigate stability and catalytic activity.

2. Experimental

2.1. $La_{0.6}Sr_{0.4}MnO_3$ Nanofibers Preparation

$Sr(NO_3)_2$ (Sigma-Aldrich, St. Louis, Missouri, USA, ACS 99+%), $La(NO_3)_3 \cdot 6H_2O$ (AlfaAesar, Haverhill, Massachusetts, USA, 99.9%), $(CH_3COO)_2Mn \cdot 4H_2O$ (Sigma-Aldrich, 99.99%) were used as metal precursors for the starting solution for electrospinning. Each precursor was carefully weighted to achieve a molar ratio 0.6:0.4 for La:Sr, and 1:1 for (La + Sr):Mn. Before mixing, the metal precursors were dissolved in a solution of 60%/40% water/ethanol. Polyvinylpyrrolidone (PVP, $M_w = 1.3 \times 10^6$ g/mol) was then added to the solution, achieving a weight ratio of 1:1.3 between the polymer and the metal salts. The PVP represented the 10% wt/wt of the whole solution. Dissolution was obtained using a magnetic stirrer for one night. The solution was then fed to the electrospinning device, equipped with a temperature and relative humidity (RH) regulator and a flat collector (Doxa Microfluidics, Malaga, Spain). The flow rate was 1 mL/h, the applied voltage was 1.7 kV/cm, RH was 40%, and the temperature was 25 °C. Next, the raw electrospun nanofiber tissue underwent heat treatment. The nanofibers were heated from room temperature to 800 °C at a constant heating rate of 0.5 °C/m. The cooling occurred without thermal control.

2.2. $La_{0.6}Sr_{0.4}MnO_3$ Powders Preparation

$La_{0.6}Sr_{0.4}MnO_3$ powders were synthesized by the citrate route [34]. Stoichiometric quantities of lanthanum nitrate ($La(NO_3)_3 \cdot 6H_2O$, Sigma-Aldrich 99.99%, powder), strontium nitrate ($Sr(NO_3)_2$, Sigma-Aldrich 99%, powder) and manganese acetate ($(CH_3COO)_2Mn \cdot 4H_2O$ (Sigma-Aldrich, 99.99%) were dissolved in deionized water and nitric acid (HNO_3). Citric acid ($C_6H_8O_7$, Sigma-Aldrich $\geq 99.0\%$) was added as a complexing agent (with a molar ratio of 1.9:1 with respect to the total amount of cations) under stirring and then the solution was led to neutral pH by dropwise addition of ammonium hydroxide. At pH 7, the stirring was stopped and the solution was heated overnight to eliminate water and to allow the formation of a gel. The gel was burnt by heating at 400 °C. The formed powders were calcined at 800 °C for 6 h using a heating and cooling ramp of 6 °C/min.

2.3. Morphological and Structural Characterization

The morphological characterization of both the LSM nanofibers and LSM powders was carried out by acquiring images through the scanning electron microscope (SEM). The SEM and energy dispersive X-ray (EDX) spectroscopy measurements were carried out with a Zeiss SUPRA 40VP using a voltage of 20 kV. A dense bulk state of the samples was set on a sample-holder by an electroconductive adhesive tape and introduced in the measurement chamber. ImageJ software (NIH, Rockville, MD, USA) was used to identify the average diameter of both LSM powder particles and LSM nanofibers, starting from the SEM images. For the LSM powder particles, only the average diameter measurement was carried out. On the contrary, for the LSM nanofibers, a tool within ImageJ called DiameterJ was used to estimate the frequency distribution of the diameter of the nanofibers. This was accomplished through a two-step process. At first, the software performed the SEM image segmentation, producing a set of black/white pictures (Figures S1 and S2 in Supplementary Materials). Then, based on the black/white images, the software computed the frequency related to each nanofiber diameter. DiameterJ was specifically used for the estimation of nanofibers' diameter distribution, and could not be used to evaluate powder particle size distribution.

X-ray photoelectron spectroscopy (XPS) measurements were carried out employing a Perkin Elmer Φ 5600 ci Multi Technique System. The calibration of the spectrometer was calculated by assuming that the binding energy (BE) of the Au 4f_{7/2} line was 84.0 eV with respect to the Fermi level. Both extended spectra (survey-187.85 eV pass energy, 0.5 eV/step, 0.05 s/step) and detailed spectra (La 3d, Mn 2p, Sr 3d, O 1s and C 1s –23.5 eV pass energy, 0.1 eV/step, 0.1 s/step) were collected with a standard Al K α source. The

atomic percentage was evaluated using PHI sensitivity factors [35] after Shirley-type background subtraction [36]. The charging effects on the peak positions were deleted by evaluating the BE differences with the C 1s peak set at 285.0 eV [37]. The samples were set in the chamber on a sample holder, on which was stuck an electroconductive adhesive tape. Bregg–Brentano geometry X-ray diffraction (XRD) analyses were performed, employing the Bruker D8 Advance diffractometer with a Cu K α radiation (40 kV, 40 mA, $\lambda = 0.154$ nm). Temperature Programmed Reduction (H₂-TPR) measurements were performed with the Autochem II 2920 Micromeritics equipped with a thermal conductivity detector (TCD). H₂-TPR measurements were carried out in a quartz reactor using 50 mg of the sample, heating from room temperature to 900 °C at 8 °C/min with a constant flow of 5% vol. H₂/Ar (50 mL/min).

2.4. Catalytic Characterization

The methane oxidation catalytic activity tests were carried out at atmospheric pressure in a quartz reactor (6 mm ID) equipped with a packed bed of the LSM powders or nanofibers under study. Temperature was increased until 800 °C with a ramp of 2 °C min⁻¹. Temperature was monitored by a thermocouple right upstream of the bed. A gas mixture of methane and air (with a stoichiometric ratio of 1:2 between methane and oxygen) was used. Flows were dosed by a Vögtlin Red-y system. The total flow of 100 mL min⁻¹ was kept constant, balancing it with He. After the reactor, water was eliminated by a cold trap. The composition of the gas mixture (before and after reaction) was measured by GC (Agilent 7890A), with a TCD detector and 13X (60/80 mesh, 1.8 m) and Porapak Q (1.8 m) columns.

3. Results and Discussion

3.1. Morphological Characterization

SEM images of LSM nanofibers and LSM powders are reported in Figure 1. Figure 1a,b shows the LSM powder particles after the sintering process. The images clearly show the presence of particles of different dimensions and shapes. Besides well-defined polyhedral crystals of more than one micron, small particles were evident. The average particle diameter, evaluated through the ImageJ software (NIH, Rockville, MD, USA), was 0.7 μ m.

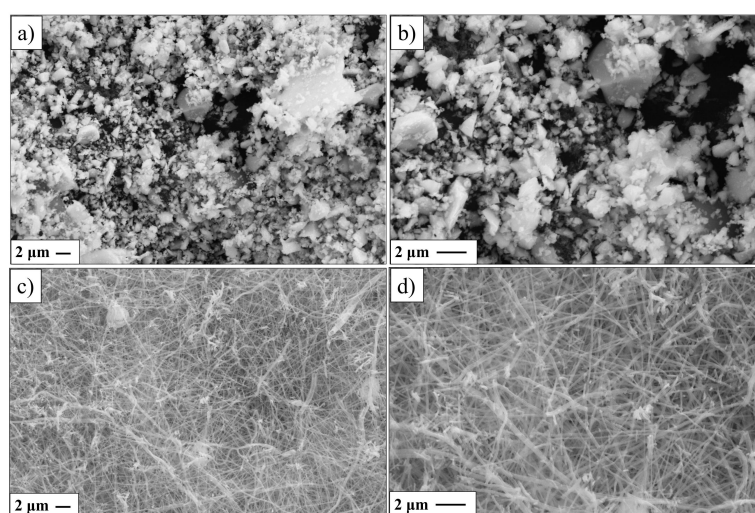


Figure 1. SEM images: (a,b) LSM powders; (c,d) LSM nanofibers.

Figure 1c,d shows the LSM nanofibers after the thermal treatment. There were thin nanofibers with no detachment, which ensured a compact network. It was possible to obtain these features after optimization of the many solution and process parameters. Indeed, as seen in Figure 1, the nanofibers showed a preferential cylindrical shape, which is the result of correct solvent evaporation during the electrospinning process. The proper evaporation of the solution was achieved by controlling three main parameters: the type of solvent,

the humidity in the electrospinning chamber, and the distance between the needle tip and the metal collector. Furthermore, the nanofibers appeared thin, but intact. This result was achieved by adding a suitable amount of polymer to the precursor solution and by optimizing the solution flow rate during the electrospinning process; essentially, the lower the amount of polymer—and the higher the flow rate—the thinner the produced fibers. Additionally, insufficient polymer quantities were shown to affect the nanofibers' ejection, provoking detachments. On the other hand, overly high flow rates require a high voltage, which would break the drop on the top of the needle, hindering the correct elongation.

The DiameterJ analysis was carried out on the SEM images of the LSM nanofibers in Figure 1c,d. Figure 2 shows, for each diameter range, the corresponding frequency, as evaluated by the software. The highest frequency was found for the diameter range 0.08–0.1 μm . Figures S1 and S2 in Supplementary Materials report the details of the DiameterJ analysis.

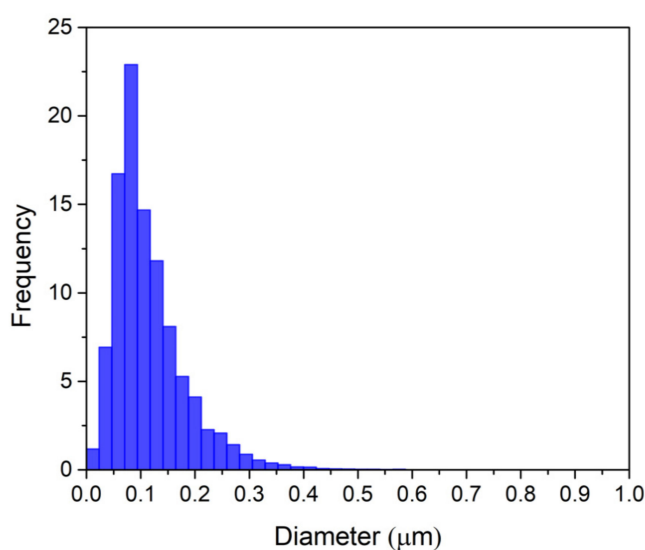


Figure 2. DiameterJ analysis of SEM images of LSM nanofibers after thermal treatment (Figure 1c,d).

XRD measurement was carried out on the heat-treated LSM nanofibers and citrate route powders to verify the achievement of the desired crystal phase. In Figure 3, the experimental patterns were reported together with the reference pattern. The experimental patterns contained all the peaks related to the reference, without any additional peaks. It confirmed that the thermal treatment permitted us to achieve crystallinity.

3.2. Chemical Characterization

Extended spectra (survey) were collected in the range of 0–1250 eV as reported in Figure 4. In the XPS survey spectra, no signals of elements other than the expected ones were detected. The atomic composition of the surface of the fibers, obtained from the XPS data, revealed a good correspondence with the nominal one (determined from the weighted amounts), as reported in Table 1.

The main difference between fibers and powders concerns the Sr/La atomic ratio. Following the nominal composition, Sr/La atomic should be 0.7. A value of 1.7 was observed in powders, whereas a value of 0.4 was detected in fibers. This suggests a marked strontium surface segregation in powders, which was not detected in fibers. Strontium segregation—with consequent formation of strontium oxide—is an undesired phenomenon that is already well-known in the literature for Sr-containing perovskites. The B-site transition metal of perovskites plays a critical role in catalytic activity, and therefore it is necessary to preserve the structure and the composition on the surface [38–40]. Furthermore, SrO is traceable to lower electronic conductivity. For all these reasons, avoiding Sr-enriched layers on LSM surface yields a substantial difference between the two syntheses and is an

important preliminary goal reached by electrospinning. Surface segregation properties of ionic solids are strongly related to their point defects. Assuming that, the presence or lack of Sr segregation on the two samples can be seen as evidence of a different presence of point defects in the two morphologies [41,42]. Further work will be spent to confirm this hypothesis.

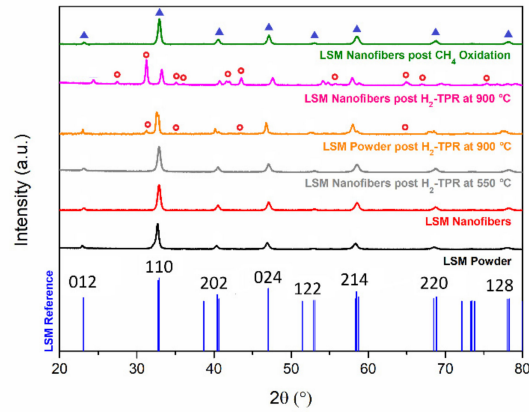


Figure 3. XRD results. The LSM reference pattern is shown in blue. Other experimental LSM patterns are as follows: powders after thermal treatment in black; electrospun nanofibers after thermal treatment in red; nanofibers after H₂-TPR performed up to 550 °C in grey and 900 °C in pink; powders after reduction in H₂ up to 900 °C in orange; and nanofibers after CH₄ oxidation up to 800 °C in green. Blue triangles refer to LSM peaks, while red circles denote MnO phase. All patterns are normalized with respect to their maximum values.

Table 1. XPS and EDX quantitative results of the atomic composition of LSM fibers and nanofibers. For better comprehension, nominal values are reported as well.

Element	Theoretical %	XPS Experimental %		EDX Experimental %	
	Nominal %	Fibers	Powders	Fibers	Powders
O	60	58	74	62	58
La	12	15	4	12	12
Sr	8	6	7	7	7
Mn	20	21	15	19	22
Mn/(La + Sr)	1	1	1.4	1	1.2
Sr/La	0.7	0.4	1.7	0.6	0.6

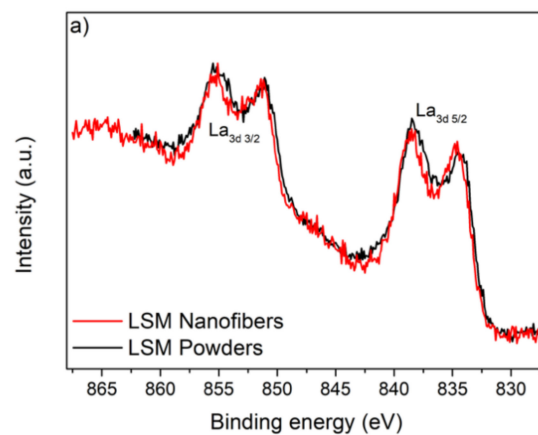


Figure 4. Cont.

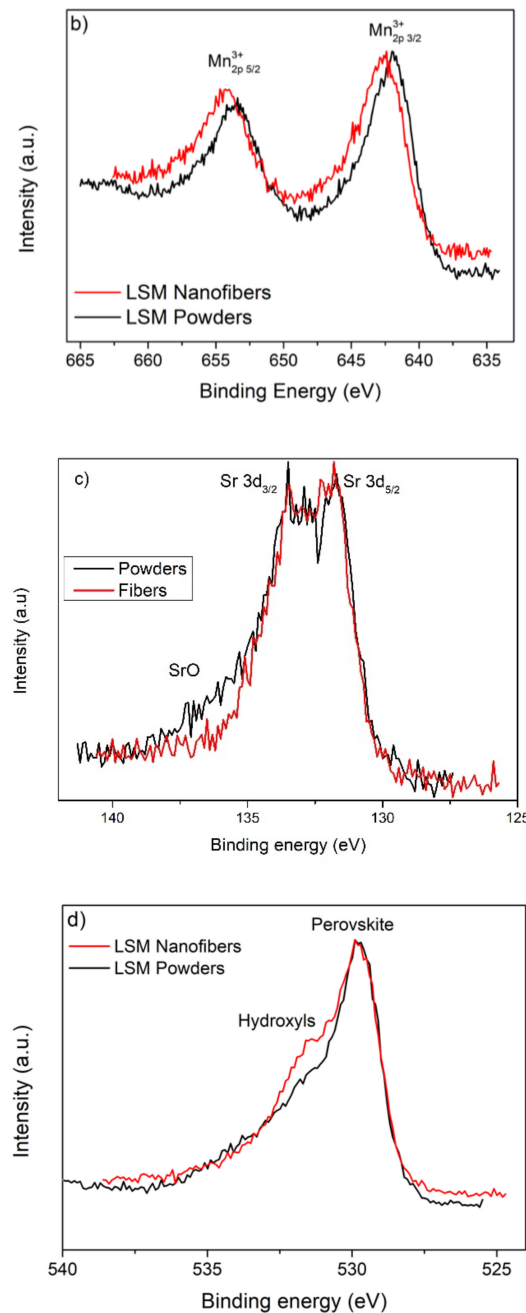


Figure 4. XPS spectra of LSM samples prepared, respectively, by citrate gel method (black line) and electrospinning (red line) (the spectra are normalized with respect to their maximum value): (a) La 3d; (b) Mn 2p; (c) Sr 3d; (d) O 1s.

La 3d peak positions (834.6 and 851.0 eV for La $3d_{5/2}$ and La $3d_{3/2}$, respectively) were consistent with those expected for this element in a perovskite powder. [43,44] The La 3d level was characterized by a double peak for each spin-orbit component, attributed either to energy loss phenomena (induced by intense O 2p \rightarrow La 4f charge transfer events) or strong final state mixing of electronic configurations [45]. The presence of the double signals was characteristic of La (III), as reported in Figure 4a. The Mn $2p_{3/2}$ spectral lines were centered in 642.4 eV, a typical position of Mn in oxides and manganites [46]. The Mn $2p_{3/2}$ peak asymmetry was due to the presence of a shake-up phenomenon for the Mn-emitted photoelectrons. This was observed, with a similar intensity, for both samples. The interpretation of the Mn 2p spectrum was complicated because of the multiple splitting

of the Mn 2p spectra of Mn⁴⁺, Mn³⁺, and Mn²⁺ ions. The exact oxidation state of Mn ions was difficult to evaluate but, according to the references [47], the observed binding energy of Mn 2p_{3/2}, suggested that the oxidation state of Mn ions was (III) and (IV) for both LSM nanofibers and powders. Overall, the higher binding energy for LSM nanofibers compared to powders (See also Table S1 in Supplementary Materials) suggested a higher presence of Mn (IV). The higher presence of the redox couple Mn^{4+/3+} in the nanofiber perovskite, as reported in Figure 4b, confirmed the Sr doping effectiveness and was in agreement with the absence of surface segregation. The stable insertion of Sr inside the perovskite cell presented a promising indication for an improvement of the material electronic conductivity. Sr 3d spectrum of LSM was fitted by the two components 3d_{5/2} and 3d_{3/2}. Their BE was in accordance with the typical values of Sr-O in perovskite (131.8–134.3 eV) [46]. A small but significant difference was observed in the spectral region Sr3d is observed. In the spectrum which referred to the powders, it was possible to observe a tail around 135–137 eV which confirmed the more relevant presence of SrO Figure 4c. The fitting results underlined that Sr from perovskite was more evident in the fibers and the contribution due to the SrO in the powders (Table S1 in Supplementary Materials). The O 1s spectra showed the presence of two contributions centered around 530 and 531.6 eV; the contribution at lower BE was attributed to the lattice oxygen, whereas the one at higher BE was attributed to surface oxygen species. This contribution was more evident in the fibers' surface, as shown in Figure 4d. The presence of hydroxyl groups on the surface of the two samples was due to the exposition of the two samples in moist air. Nevertheless, the presence of these chemical species on the surface was not relevant to this study, since they were easily removed by heating the material during the catalytic analysis.

An EDX analysis was carried out to better understand the chemical composition in the inner region of the nanofibers. Table 1 shows the comparison between the nominal and the experimentally detected percentages of the two samples. No marked differences were present between fibers and powders with the nominal values, confirming that the two syntheses were successfully realized, and the Sr segregation was limited to a few surface monolayers. It is possible to assert, thus, that the two samples differed in morphology and in the chemical composition of their surfaces.

3.3. Temperature Programmed Reduction (H₂-TPR) and N₂-Adsorption-Desorption

The TPR profiles obtained for the fibers and the powders, as compared in Figure 5, showed two peaks, one at 430 °C and the other at 700 °C. Both were related to manganese cation reduction, since manganese is the only species that can be reduced in the analyzed temperature range. The lower temperature peak corresponded to the reduction of Mn⁴⁺, while the second was due to the reduction from Mn³⁺ to Mn²⁺. This hypothesis, suggested in the literature [48], was also confirmed by the XRD measurements performed after H₂-TPR. In the XRD patterns obtained after TPR, MnO was observed, but the main part of the sample maintained the perovskite structure. In Figure 3, the XRD pattern obtained for the fibers' sample reduced up to 550 °C (hypothetically, when the first reduction was finished, but the second one had still to start) underlined the absence of the MnO phase. This result confirmed that the peak at the higher temperature was due to the reduction to Mn²⁺.

The experimental hydrogen consumption of a mole of fibers is about 9×10^{-5} mol, which is lower than the theoretical one (16.7×10^{-5} mol/mol). This was calculated assuming that all the Sr inserted in the sample promoted the manganese to Mn⁴⁺, and all manganese was reduced to Mn²⁺. This assumption was disproved, however, as the XRD after TPR showed LSM phase presence. Indeed, a simple calculation showed that about 50% of the Mn in the sample was reduced to Mn²⁺. In addition, in order to understand whether the different morphology modified the stability, the same reducing treatment (5% H₂ in Ar at 900°) was performed on the powders. Significant differences were noted in the TPR profiles. The peak referring to Mn^{4+/3+} reduction started at 305 °C for powders, or 35 °C higher than for nanofibers. Furthermore, the Mn^{3+/2+} peak was much higher for nanofibers than for powders. These two results indicated that nanofibers featured a higher

reactivity. The post-reduction XRD was also significantly different. From Figure 3, it is possible to note how the powder diffractogram showed the same reflexes after reduction of MnO observed in the fibers, but with a lower intensity. The different behaviors observed between powders and fibers suggested lower reducibility of the powders. This could be explained by considering two aspects: first, the high presence of SrO on the powder's surface, which behaved like a coating for the perovskitic structure, protecting it from reduction; and second, the higher surface area observed for the fibers.

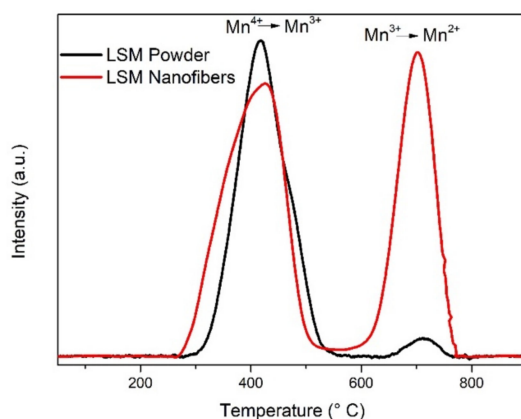


Figure 5. TPR profile of LSM nanofibers and powders. The patterns are normalized with respect to their maximum values.

Figure 6 shows the N₂-adsorption-desorption isotherms carried out on LSM nanofibers and powders. The BET plots of the two samples were both tracible to type IV isotherms, since they showed a hysteresis cycle between the adsorption and desorption processes. Therefore, at the same partial pressure, during the desorption, more nitrogen was desorbed than gas adsorbed in the adsorption process. The hysteresis served as a signal of a mesoporous material, but the small region between adsorption and desorption curves indicated that there was little dispersion of the average width of the pores [49]. The BET isotherms made it possible to determine the BET surface area. The surface area calculated for the LSM nanofibers was 16.7 m²/g. A good correspondence with other studies in the literature could be observed in this material [50]. This value more than doubled the surface area calculated for the LSM powders (5.8 m²/g). The latter was in line with the typical values for LSM perovskite powders synthesized by the citrate route and treated at the same calcination temperature (800 °C). The high BET surface area obtained for the LSM nanofibers, together with the absence of Sr-segregation, could explain the low hydrogen stability found at high temperatures in the TPR measurements.

3.4. Methane Oxidation Catalytic Activity Test

The catalytic results obtained with LSM nanofibers and powders are reported in Figure 7. A GC analysis of the reaction products, carried out after water condensation, showed that the molar ratio between the produced CO₂ and the consumed CH₄ was 1:1. No other reaction products were detected by the instrument. Therefore, since there was a full correspondence between methane consumption and CO₂ production, the complete oxidation of methane was confirmed. For the nanofibers, the onset temperature for methane oxidation was about 500 °C; for powders, it was 100 °C higher. The temperature of 50% methane conversion was lower for nanofibers (700 °C) than powders (900 °C). For the nanofibers, the maximum conversion was about 75% at 800 °C. Considering that the typical temperature range for SOFCs application was between 600 °C and 800 °C, it could be argued that this catalytic activity of nanofibers could be exploited in relationship with their application in these devices. Taking into account the catalytic results and the previous material characterizations, the higher activity of nanofibers could have two different

explanations. The first is the higher surface area of nanofibers (compared to powders) and, consequently, the higher number of active sites for the reaction. In addition, the higher performance of nanofibers could be explained by the previous XPS results. Indeed, SrO in the LSM powders surface was inactive to methane oxidation and covered the underneath of the perovskite structure. On the contrary, electrospinning synthesis made it possible to maintain the active perovskite phase up until the last atomic layers. Figure 3 compares the XRD patterns obtained for the nanofiber samples as-synthesized and after the reaction. No differences were detectable considering either the position of the peaks or their FWHM. Thus, no modification regarding the phase structure or crystallinity was attributable to the performed catalytic test.

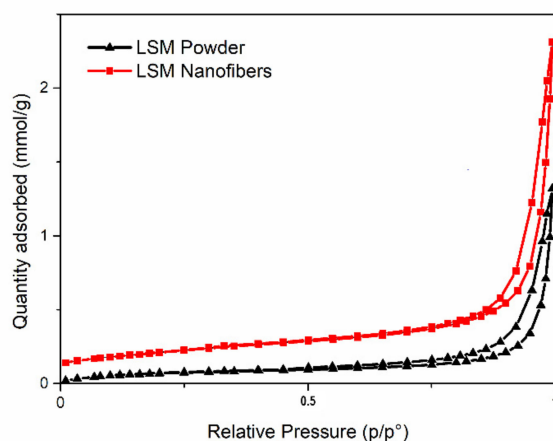


Figure 6. N₂-adsorption and desorption isotherms for LSM powders (black) and nanofibers (red).

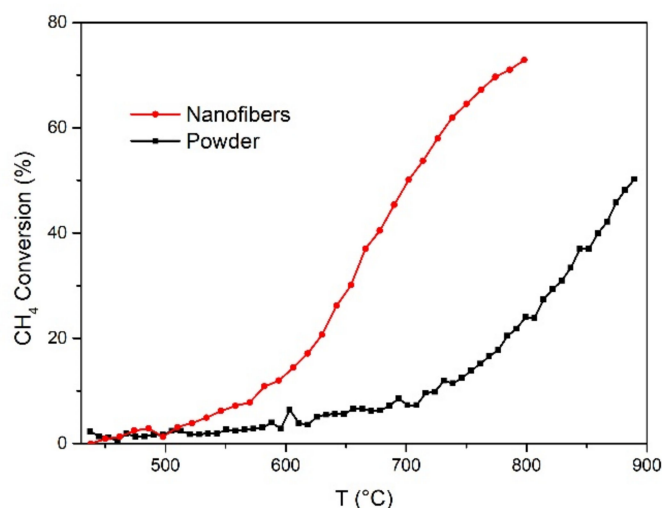


Figure 7. Catalytic activity in methane oxidation measured for LSM powders (black) and nanofibers (red).

4. Conclusions

La_{0.6}Sr_{0.4}MnO₃ (LSM), the SOFC cathode state-of-the-art material, was prepared in the form of nanofibers and powders. Proper synthesis and crystallinity were confirmed for both samples by XRD. The X-ray photoelectron spectroscopy (XPS) measurements showed that the two different synthesis routes heavily influenced the surface properties, since LSM powders displayed strontium oxide segregation, which was not detected in nanofibers. The catalytic activity toward direct methane oxidation was investigated for the two samples, showing that the onset temperature for methane oxidation was 500 °C with nanofibers, and 600 °C with powders. Methane conversion at 800 °C was 73% with nanofibers and 50%

at 900 °C with powders. Two explanations were proposed for the superior performance of nanofibers; first, the absence of strontium oxide segregation on the surface, which exhibited perovskitic active sites up until the last atomic layers; and second, the higher surface area (as revealed by BET analysis). Since the typical working temperature range for IT-SOFCs is 600–800 °C, the structural and catalytic characterizations performed in this work support the possibility of using LSM nanofibers on the anode side. This is particularly relevant, since it paves the way for the development of symmetric IT-SOFCs.

Supplementary Materials: The following are available online at <https://www.mdpi.com/article/10.3390/en14123602/s1>, Figure S1: Example of ImageJ segmentation process. In the left top corner, the original SEM picture is reported. The other images are the black/white segmented images. Figure S2: Example of ImageJ diameter location process. The red lines represent the central axes of the nanofibers in one of the segmented images. Figure S3: Fitting curves for the different element lines studied in this work. From top to bottom: O1s, La3d, Sr3d, Mn2p. On the left there are the powders spectra, while on the right those for fibers. Table S1: Fitting parameters of the different studied orbitals.

Author Contributions: Materials preparation, E.S. and C.S.; investigation, E.S. and C.S.; resources, A.G. and P.C.; data curation, E.S. and C.S.; writing—original draft preparation, E.S. and C.S.; writing—review, A.G. and P.C.; supervision, A.G. and P.C.; funding acquisition, A.G. and P.C. All authors have read and agreed to the published version of the manuscript.

Funding: The part of this research carried out at the University of Genoa (Italy) received financial support from the San Paolo Project ‘COELUS-Production of renewable fuel by CO-Electrolysis and reUse of carbon dioxide’ (ID ROL 32604).

Acknowledgments: C.S. and P.C. at the University of Genoa (Italy) acknowledge financial support from the San Paolo Project ‘COELUS-Production of renewable fuel by CO-Electrolysis and reUse of carbon dioxide’ (ID ROL 32604).

Conflicts of Interest: The authors declare no conflict of interest.

References

1. da Silva, F.S.; de Souza, T.M. Novel materials for solid oxide fuel cell technologies: A literature review. *Int. J. Hydrogen Energy* **2017**, *42*, 26020–26036. [[CrossRef](#)]
2. Huang, K.; Goodenough, J.B. *Solid Oxide Fuel Cell Technology*; Woodhead Publishing Limited: Cambridge, UK, 2009.
3. Mehmeti, A.; McPhail, S.J.; Pumiglia, D.; Carlini, M. Life cycle sustainability of solid oxide fuel cells: From methodological aspects to system implications. *J. Power Sources* **2016**, *325*, 772–785. [[CrossRef](#)]
4. Stambouli, A.; Traversa, E. Solid oxide fuel cells (SOFCs): A review of an environmentally clean and efficient source of energy. *Renew. Sustain. Energy Rev.* **2002**, *6*, 433–455. [[CrossRef](#)]
5. Kaur, P.; Singh, K. Review of perovskite-structure related cathode materials for solid oxide fuel cells. *Ceram. Int.* **2020**, *46*, 5521–5535. [[CrossRef](#)]
6. Panthi, D.; Choi, B.; Tsutsumi, A. Direct methane operation of a micro-tubular solid oxide fuel cell with a porous zirconia support. *J. Solid State Electrochem.* **2017**, *21*, 255–262. [[CrossRef](#)]
7. Costamagna, P.; Costa, P.; Antonucci, V. Micro-modelling of solid oxide fuel cell electrodes. *Electrochim. Acta* **1998**, *43*, 375–394. [[CrossRef](#)]
8. Tu, B.; Yin, Y.; Zhang, F.; Su, X.; Lyu, X.; Cheng, M. High performance of direct methane-fuelled solid oxide fuel cell with sa-marium modified nickel-based anode. *Int. J. Hydrogen Energy* **2020**, *45*, 27587–27596. [[CrossRef](#)]
9. Park, S.; Craciun, R.; Vohs, J.M.; Gorte, R.J. Direct oxidation of sulfur-containing fuels in a solid oxide fuel cell. *J. Electrochem. Soc.* **1999**, *146*, 3603–3605. [[CrossRef](#)]
10. Liu, J.; Madsen, B.D.; Ji, Z.; Barnett, S.A. A Fuel-Flexible Ceramic-Based Anode for Solid Oxide Fuel Cells. *Electrochem. Solid-State Lett.* **2002**, *5*, A122–A124. [[CrossRef](#)]
11. Grgicak, C.M.; Green, R.G.; Giorgi, J.B. SOFC anodes for direct oxidation of hydrogen and methane fuels containing H₂S. *J. Power Sources* **2008**, *179*, 317–328. [[CrossRef](#)]
12. Perry Murray, E.; Tsai, T.; Barnett, S.A. A direct-methane fuel cell with a ceria-based anode. *Nature* **1999**, *400*, 649–651. [[CrossRef](#)]
13. Yang, G.; Jung, W.; Ahn, S.-J.; Lee, D. Controlling the Oxygen Electrocatalysis on Perovskite and Layered Oxide Thin Films for Solid Oxide Fuel Cell Cathodes. *Appl. Sci.* **2019**, *9*, 1030. [[CrossRef](#)]
14. Jiang, S.P. Development of lanthanum strontium cobalt ferrite perovskite electrodes of solid oxide fuel cells—A review. *Int. J. Hydrogen Energy* **2019**, *44*, 7448–7493. [[CrossRef](#)]

15. Richter, J.; Holtappels, P.; Graule, T.; Nakamura, T.; Gauckler, L.J. Materials design for perovskite SOFC cathodes. *Monatshefte Chem. Chem. Mon.* **2009**, *140*, 985–999. [[CrossRef](#)]
16. Jun, A.; Kim, J.; Shin, J.; Kim, G. Perovskite as a Cathode Material: A Review of its Role in Solid-Oxide Fuel Cell Technology. *ChemElectroChem* **2016**, *3*, 511–530. [[CrossRef](#)]
17. Escudero, M.; Irvine, J.; Daza, L. Development of anode material based on La-substituted SrTiO₃ perovskites doped with manganese and/or gallium for SOFC. *J. Power Sources* **2009**, *192*, 43–50. [[CrossRef](#)]
18. Mailadil, T.S. ABO₃ type perovskites. In *Dielectric Materials for Wireless Communication*; Elsevier Science: Amsterdam, The Netherlands, 2008.
19. Jiang, S.P. Development of lanthanum strontium manganite perovskite cathode materials of solid oxide fuel cells: A review. *J. Mater. Sci.* **2008**, *43*, 6799–6833. [[CrossRef](#)]
20. Farrell, B.L.; Linic, S. Oxidative coupling of methane over mixed oxide catalysts designed for solid oxide membrane reactors. *Catal. Sci. Technol.* **2016**, *6*, 4370–4376. [[CrossRef](#)]
21. Chen, X.J.; Liu, Q.L.; Khor, K.A.; Chan, S.H. High-performance (La,Sr)(Cr,Mn)O₃/(Gd,Ce)O_{2-δ} composite anode for direct oxidation of methane. *J. Power Sources* **2007**, *165*, 34–40. [[CrossRef](#)]
22. Costamagna, P.; Sanna, C.; Campodonico, A.; Sala, E.M.; Sažinas, R.; Holtappels, P. Electrochemical Impedance Spectroscopy of Electrospun La_{0.6}Sr_{0.4}Co_{0.2}Fe_{0.8}O_{3-Δ} Nanorod Cathodes for Intermediate Temperature–Solid Oxide Fuel Cells. *Fuel Cells* **2019**, *19*, 472–483.
23. Enrico, A.; Zhang, W.; Traulsen, M.L.; Sala, E.M.; Costamagna, P.; Holtappels, P. La_{0.6}Sr_{0.4}Co_{0.2}Fe_{0.8}O_{3-δ} nanofiber cathode for intermediate-temperature solid oxide fuel cells by water-based sol-gel electrospinning: Synthesis and electrochemical behaviour. *J. Eur. Ceram. Soc.* **2018**, *38*, 2677–2686. [[CrossRef](#)]
24. Sanna, C.; Zhang, W.; Costamagna, P.; Holtappels, P. Synthesis and electrochemical characterization of electrospun nanofiber cathodes for intermediate-temperature solid oxide fuel cells. *Int. J. Hydrogen Energy* **2020**, *46*, 13818–13831. [[CrossRef](#)]
25. Zhao, E.; Liu, X.; Liu, L.; Huo, H.; Xiong, Y. Effect of La_{0.8}Sr_{0.2}Co_{0.2}Fe_{0.8}O_{3-δ} morphology on the performance of composite cathodes. *Prog. Nat. Sci. Mater. Int.* **2014**, *24*, 24–30. [[CrossRef](#)]
26. Jeon, Y.; Myung, J.H.; Hyun, S.H.; Shul, Y.G.; Irvine, J.T. Corn-cob like nanofibres as cathode catalysts for an effective microstructure design in solid oxide fuel cells. *J. Mater. Chem. A* **2017**, *5*, 3966–3973. [[CrossRef](#)]
27. Koo, J.Y.; Lim, Y.; Kim, Y.B.; Byun, D.; Lee, W. Electrospun yttria-stabilized zirconia nanofibers for low-temperature solid oxide fuel cells. *Int. J. Hydrogen Energy* **2017**, *42*, 15903–15907. [[CrossRef](#)]
28. Fan, L.; Xiong, Y.; Liu, L.; Wang, Y.; Kishimoto, H.; Yamaji, K.; Horita, T. Performance of Gd_{0.2}Ce_{0.8}O_{1.9} infiltrated La_{0.2}Sr_{0.8}TiO₃ nanofiber scaffolds as anodes for solid oxide fuel cells. *J. Power Sources* **2014**, *265*, 125–131. [[CrossRef](#)]
29. Zhang, W. Electrospinning for Solid Oxide Fuel Cells. In *Electrospinning for Advanced Energy and Environmental Applications*; CRC Press; Taylor & Francis Group: Boca Raton, FL, USA, 2016.
30. Teo, W.E.; Ramakrishna, S. A review on electrospinning design and nanofibre assemblies. *Nanotechnology* **2006**, *17*, R89–R106. [[CrossRef](#)]
31. Deitzel, J.; Kleinmeyer, J.; Harris, D.; Tan, N.B. The effect of processing variables on the morphology of electrospun nanofibers and textiles. *Polymer* **2001**, *42*, 261–272. [[CrossRef](#)]
32. Aruna, S.; Balaji, L.; Kumar, S.S.; Prakash, B.S. Electrospinning in solid oxide fuel cells—A review. *Renew. Sustain. Energy Rev.* **2017**, *67*, 673–682. [[CrossRef](#)]
33. Costamagna, P.; Holtappels, P.; Sanna, C. Metal Oxide Nanofiber-Based Electrodes in Solid Oxide Fuel Cells. In *Metal Oxide-Based Nanofibers Their Applications*; Elsevier: Amsterdam, The Netherlands, in press.
34. Marcilly, C.; Courty, P.; Delmon, B. Preparation of highly dispersed mixed oxides and oxide solid solutions. *J. Am. Ceram. Soc.* **1970**, *53*, 56. [[CrossRef](#)]
35. Moulder, J.F.; Stickle, W.F.; Sobol, P.E.; Bomben, K.D. *Handbook of X-ray Photoelectron Spectroscopy*; Perkin-Elmer Corporation: Waltham, MA, USA, 1992.
36. Mills, K.A.; Davis, R.F.; Kevan, S.D.; Thornton, G.; Shirley, D.A. Angle-resolved photoemission determination of Δ-line valence bands in Pt and Au using synchrotron radiation. *Phys. Rev. B* **1980**, *22*, 581–592. [[CrossRef](#)]
37. Wagner, C.D.; Riggs, W.M.; Davis, L.E.; Moulder, J.F.; Muilenberg, G.E. *Handbook of X-ray Photoelectron Spectroscopy*; Perkin-Elmer Corp., Physical Electronics Division: Eden Prairie, MN, USA, 1979.
38. Wu, Q.H.; Liu, M.; Jaegermann, W. X-ray photoelectron spectroscopy of LaSrMnO₃. *Mater. Lett.* **2005**, *59*, 1980–1983. [[CrossRef](#)]
39. Caillol, N.; Pijolat, M.; Siebert, E. Investigation of chemisorbed oxygen, surface segregation and effect of post-treatments on La_{0.8}Sr_{0.2}MnO₃ powder and screen-printed layers for solid oxide fuel cell cathodes. *Appl. Surf. Sci.* **2007**, *253*, 4641–4648. [[CrossRef](#)]
40. Jiang, S.P.; Love, J.G.; Zhang, J.P.; Hoang, M.; Ramprakash, Y.; Hughes, A.E.; Badwal, S.P.S. The electrochemical performance of LSM/zirconia-yttria interface as a function of a-site non-stoichiometry and cathodic current treatment. *Solid State Ion.* **1999**, *121*, 1–10. [[CrossRef](#)]
41. Horvath, G.; Gerblinger, J.; Meixner, H.; Giber, J. Segregation driving forces in perovskite titanates. *Sens. Actuators B Chem.* **1996**, *32*, 93–99. [[CrossRef](#)]
42. Nowotny, J. Interface defect chemistry of oxide ceramic materials. *Solid State Ion.* **1991**, *49*, 119–128. [[CrossRef](#)]
43. Glisenti, A.; Galenda, A.; Natile, M.M. LaMnO₃: Influence of the Addition of Ba and Sr. *Surf. Sci. Spectra* **2009**, *16*, 83. [[CrossRef](#)]

44. Natile, M.M.; Ugel, E.; Maccato, C.; Glisenti, A. LaCoO₃: Effect of synthesis conditions on properties and reactivity. *Appl. Catal. B Environ.* **2007**, *72*, 351–362. [[CrossRef](#)]
45. Vasquez, R.P. X-ray photoemission measurements of La_{1-x}Ca_xCoO₃ (x = 0, 0.5). *Phys. Rev. B* **1996**, *54*, 14938–14941. [[CrossRef](#)] [[PubMed](#)]
46. Berger, D.; Matei, C.; Papa, F.; Macovei, D.; Fruth, V.; Deloume, J.P. Pure and doped lanthanum manganites obtained by combustion method. *J. Eur. Ceram. Soc.* **2007**, *27*, 4395–4398. [[CrossRef](#)]
47. Murray, J.W.; Dillard, J.G.; Giovanoli, R.; Moers, H.; Stumm, W. Oxidation of Mn(II): Initial mineralogy, oxidation state and ageing. *Geochim. Cosmochim. Acta* **1985**, *49*, 463–470. [[CrossRef](#)]
48. Florea, M.; Somacescu, S.; Postole, G.; Urda, A.; Neatu, F.; Neatu, S.; Massin, L.; Gelin, P. La_{0.75}Sr_{0.25}XO₃ (X = Fe, Mn or Cr) with coking tolerance for CH₄/H₂O reaction: Effect of H₂S on catalytic performance. *Catal. Sci. Technol.* **2019**, *9*, 2351–2366. [[CrossRef](#)]
49. Dollimore, D.; Spooner, P.; Turner, A.D. The bet method of analysis of gas adsorption data and its relevance to the calculation of surface areas. *Surf. Technol.* **1976**, *4*, 121–160. [[CrossRef](#)]
50. Chen, Y.; Bu, Y.; Zhang, Y.X.; Yan, R.; Ding, D.; Zhao, B.; Yoo, S.; Dang, D.; Hu, R.; Yang, C.; et al. A Highly Efficient and Robust Nanofiber Cathode for Solid Oxide Fuel Cells. *Adv. Energy Mater.* **2017**, *7*, 1601890. [[CrossRef](#)]